ARTICLE

Check for updates

Observing light-induced Floquet band gaps in the longitudinal conductivity of graphene

Lukas Broers [1,2✉] & Ludwig Mathey[1,2,3]

Floquet engineering presents a versatile method of dynamically controlling material properties. The light-induced Floquet-Bloch bands of graphene feature band gaps, which have not yet been observed directly. We propose optical longitudinal conductivity as a realistic observable to detect light-induced Floquet band gaps in graphene. These gaps manifest as resonant features in the conductivity, when resolved with respect to the probing frequency and the driving field strength. The electron distribution follows the light-induced Floquet-Bloch bands, resulting in a natural interpretation as occupations of these bands. Furthermore, we show that there are population inversions of the Floquet-Bloch bands at the band gaps for sufficiently strong driving field strengths. This strongly reduces the conductivity at the corresponding frequencies. Therefore our proposal puts forth not only an unambiguous demonstration of light-induced Floquet-Bloch bands, which advances the field of Floquet engineering in solids, but also points out the control of transport properties via light, that derives from the electron distribution on these bands.

[1] Center for Optical Quantum Technologies, University of Hamburg, Hamburg, Germany. [2] Institute for Laser Physics, University of Hamburg, Hamburg, Germany. [3] The Hamburg Center for Ultrafast Imaging, Hamburg, Germany. ✉email: lbroers@physnet.uni-hamburg.de

Controlling solids with light constitutes a modern approach to induce novel functionalities. A specific framework within this broader effort is Floquet engineering. Floquet engineering refers to inducing dynamics that are captured by an effective Floquet Hamiltonian in a system by periodic driving. For a non- or weakly interacting system this approach describes effective single-particle states that form a natural basis for the driven system. These states are the Floquet-Bloch bands of the electrons, in analogy to the Bloch bands of the equilibrium system. These Floquet-Bloch bands can have qualitatively distinct features from the Bloch bands of the non-driven system[1–4]. A striking example are Floquet topological insulators[5–7], for which applications in spintronics[8] have been discussed. A general overview on spintronics can be found in[9]. A specific realization of Floquet topological insulators is monolayer graphene illuminated with circularly polarized light, for which the band structure approaches the Haldane model in the high-frequency limit[10,11]. However, while the ground state of the equilibrium Haldane model forms indeed a topological insulator, which manifests in a quantized Hall conductance, the Hall conductance of optically driven graphene is not topologically quantized, but of geometric-dissipative origin[12,13]. This observation is part of the larger challenge of an unambiguous detection of the Floquet-Bloch bands in a solid. We note that the geometric properties of bands in periodically driven lattices have been demonstrated in ultracold atom experiments[14–16] as well as helical wave guides[17,18] and classical settings[19]. Signatures of Floquet-Bloch bands have been seen in angle-resolved photoelectron spectroscopy[20] and approaches for observing related pseudospin textures have been proposed[21,22]. In this context, the effects of Auger recombination[23] and scattering decoherence[24] on the electron dynamics in graphene have been discussed. The transport properties of similar Floquet systems have been discussed[25] and the high-frequency probing limit has been explored[26]. However, a smoking-gun in the transport measurements of solids is lacking.

In this paper, we propose to detect light-induced Floquet band gaps in graphene via the optical longitudinal transport. We determine the optical conductivity as a function of the probing frequency and the driving field strength, which displays resonant features. We present an interpretation of these features in terms of the Floquet-Bloch band dispersion and the effective occupation of these states. These occupations are determined by the dissipation and the driving field, which balance out to form the steady state. We include the dissipation processes in our master equation approach that we use to describe the system. With this, we attribute the observable resonant features in the optical conductivity to two transition processes. One occurs between bands inside the same Floquet zone and the other between adjacent bands of neighboring Floquet zones. These processes compete in their impact on the optical conductivity, which can result in vanishing and even negative optical conductivity for specific frequencies and driving field strengths. In general, we show that the conductivity depends on the relative occupation of the Floquet bands. We also point out that the relative occupation is in qualitative agreement with a comoving band velocity, to be defined below. In particular, we show that there are regimes of driving field strengths that show an effective inversion of Floquet band populations. These are in the regimes in which negative optical conductivity is achieved. Therefore, as a second point besides the demonstration of Floquet-Bloch bands in solids, our proposal shows non-trivial control of the transport properties of solids, induced by light.

Results and discussion

Model Hamiltonian. We consider a circularly polarized laser with frequency $\omega_d = 2\pi \times 48$ THz ≈ 200 meV and variable field strength E_d, which illuminates a graphene layer from

perpendicular direction. The electromagnetic forces drive the electrons into a steady state. We propose to measure the longitudinal AC conductivity of this steady state in the optical frequency domain. The conductivity displays frequency regimes in which its magnitude is increased compared to the non-driven graphene layer, and regimes in which it is decreased. These frequency regimes derive from resonances between the Floquet states, which in turn depend on the driving field strength. As a result, these frequency regimes can be tuned to overlap, resulting in a partial cancellation. In particular, the band gap Δ_0 at the Dirac point can be overshadowed, in general, by other features. However, we point out a regime in which it can be identified unambiguously.

The Hamiltonian of light-driven graphene, close to the Dirac point is given by

$$H = \sum_k c_{\mathbf{k}}^{\dagger} \mathbf{h}(\mathbf{k}) c_{\mathbf{k}}, \tag{1}$$

where $c_{\mathbf{k}} = (c_{\mathbf{k},A}, c_{\mathbf{k},B})^{\mathrm{T}}$ and $c_{\mathbf{k},i}$ are the fermionic annihilation operators of an electron with momentum $\mathbf{k}$ and sublattice index $i = A, B$. Invoking the edge-bulk correspondance, the transport properties of the periodic bulk captured by Eq. (1) directly translate to localized edge modes of finite systems. The Hamiltonian of a single momentum $\mathbf{k}$ is

$$\mathbf{h}(\mathbf{k}) = \hbar v_{\mathrm{F}}(q_x \sigma_x + q_y \sigma_y), \tag{2}$$

with

$$q_x = k_x + \frac{E_d}{\omega_d}\sin(\omega_d t) - \frac{E_L}{\omega_L}\cos(\omega_L t), \tag{3}$$

$$q_y = k_y + \frac{E_d}{\omega_d}\cos(\omega_d t), \tag{4}$$

where $v_{\mathrm{F}} \approx 10^6$ m s^{-1} is the Fermi velocity. k_i are the momentum components and σ_i are the Pauli matrices. E_d and ω_d are field strength and frequency of the driving laser. E_L and ω_L are the same quantities for the longitudinal probing field.

We simulate the dynamics via a master equation approach, expanding on previous work by some of the authors[12]. The density matrix of the system factorizes in momentum space, as $\rho = \prod_k \rho_k$. Each ρ_k matrix operates on a four dimensional Hilbert space, given by the states $|0\rangle$, $c_{\mathbf{k},A}^{\dagger}|0\rangle$, $c_{\mathbf{k},B}^{\dagger}|0\rangle$, $c_{\mathbf{k},B}^{\dagger}c_{\mathbf{k},A}^{\dagger}|0\rangle$. We include doubly and unoccupied states to determine two-time correlation functions, and thereby frequency-resolved quantities.

In addition to the unitary time evolution induced by the Hamiltonian in Eq. (2), we include dissipation via Lindblad operators defined in the instantaneous eigenbasis of the driven system, to describe the dissipative environment due to degrees of freedom not included in the Hamiltonian. We include a dephasing term γ_z, a decay term γ_- and a term with decay rate γ_{bg} that models particle exchange of the graphene layer to a supporting substrate backgate. This model provides a realistic discription of the non-equilibrium electron dynamics[12].

We choose the coefficients $\gamma_z = 1$ THz, $\gamma_- = 2.25$ THz and $\gamma_{\mathrm{bg}} = 2.5$ THz. This sets the scale for the broadening of the effective bands in the single-particle correlation function as well as the optical conductivity. These values are a factor of 10 smaller than those estimated[12] for the experimental setup of McIver et al.[13]. Our predictions apply to high-mobility samples, e.g., BN-encapsulated graphene. For larger values, such as those that are realized in the work of McIver et al.[13], resolving the gap features that we describe in the following, would require larger driving frequencies and stronger driving. Throughout this work we use the temperature $T = 80$ K, which is the same as the setup of
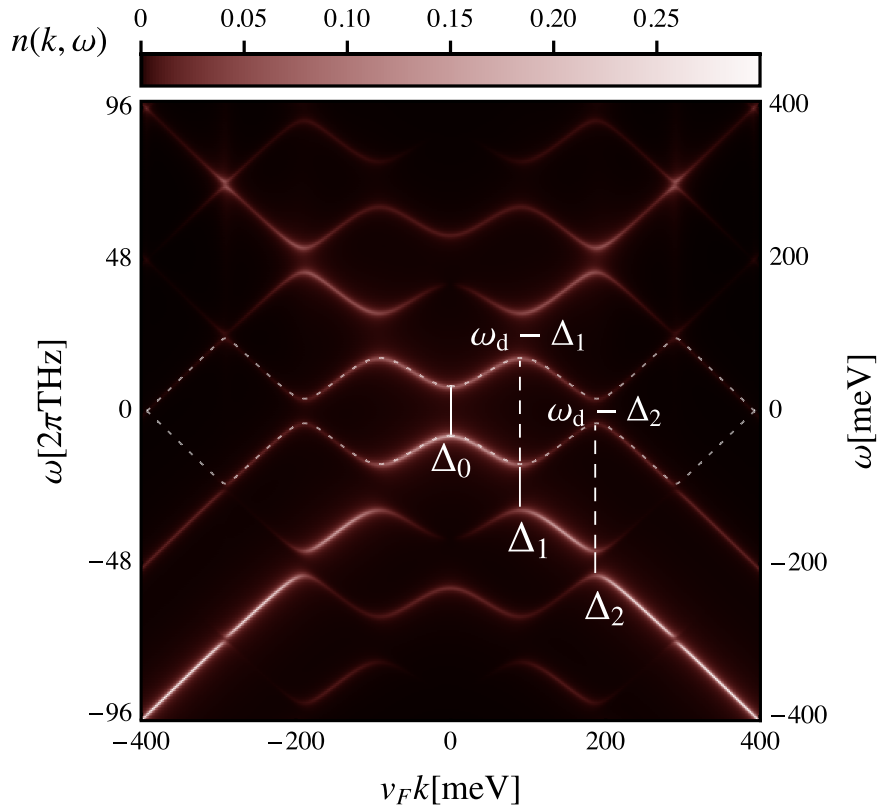
Fig. 1 Electron distribution of light-driven graphene, revealing its Floquet states. The electron distribution $n(\mathbf{k}, \omega)$ of graphene driven with circularly polarized light at the driving frequency $\omega_d = 2\pi \times 48$ THz ≈ 200 meV and field strength $E_d = 26$ MV m^{-1}. The distribution $n(\mathbf{k}, \omega)$ depends only on the momentum $k = |\mathbf{k}|$. This quantity displays the steady state occupation of the Floquet-Bloch band structure. The one-photon resonance gap Δ_1 at $k = \omega_d/(2v_F)$, the two-photon gap Δ_0 at the Dirac point, and the two-photon gap at $k = \omega_d/v_F$ are highlighted for clarity. v_F is the Fermi velocity. Additionally, the complementary gaps $\omega_d - \Delta_1$ and $\omega_d - \Delta_2$ are indicated. The dotted lines indicate the Floquet energies of the first Floquet zone.

McIver et al.[13]. We fix the value of the chemical potential at $\mu = 0$.

Electron distribution. As a first observable we display the momentum-resolved and energy-resolved electron distribution inspired by Freericks et al.[27]

$$n(\mathbf{k}, \omega) = \int_{\tau_1}^{\tau_2} \int_{\tau_1}^{\tau_2} \mathcal{G}(\mathbf{k}, t_2, t_1) \frac{e^{i\omega(t_2 - t_1)}}{(\tau_2 - \tau_1)^2} \, dt_2 dt_1, \qquad (5)$$

which is manifestly real-valued with

$$\mathcal{G}(\mathbf{k}, t_2, t_1) = \langle c_{\mathbf{k},A}^\dagger(t_2) c_{\mathbf{k},A}(t_1) \rangle + \langle c_{\mathbf{k},B}^\dagger(t_2) c_{\mathbf{k},B}(t_1) \rangle \qquad (6)$$

for which its complex conjugate corresponds to the exchange of t_1 and t_2. We use the time interval $[\tau_1, \tau_2]$ as the probing interval. We choose τ_1 such that the system has reached its steady state. $\tau_2 - \tau_1$ is a sufficiently long probing time of the order of hundreds of driving periods $2\pi/\omega_d$ that is also commensurate with the probing period $2\pi/\omega_L$. We note that this quantity provides a prediction for trARPES measurements[27]. In Fig. 1 we show $n(k = |\mathbf{k}|, \omega)$ for the driving field strength $E_d = 26$ Me V m^{-1}. We note that a similar result was presented in previous work by some of the authors[12]. The electron distribution of the steady state is consistent with the effective band structure predicted by Floquet theory and identifies the non-equilibrium electron occupation of these Floquet-Bloch bands.

We label the band gaps as Δ_m, based on their location $m\omega_d/(2v_F)$ in momentum space for small driving field strength $E_d \to 0$, as shown in Fig. 1. Due to the periodicity in frequency space of the Floquet spectrum, there is a complementary gap $\omega_d - \Delta_m$ for any given band gap Δ_m, with $m > 0$. These complementary gaps

are also visible in the optical conductivity of the system. They reduce the conductivity at the corresponding frequency, rather than enhance it. The gap Δ_0 at the Dirac point does not exhibit this behavior, as discussed later.

Optical conductivity. The second observable that we present is the longitudinal optical conductivity. We propose to measure this quantity experimentally, to compare to the predictions made here. In Fig. 2 we show the real part of the total optical conductivity of the system as a function of the driving field strength E_d. This is obtained from our master equation approach as

$$\sigma_r(\omega_L) = \text{Re}\left[\frac{j_x(\omega_L)}{E_x(\omega_L)}\right], \qquad (7)$$

with the longitudinal current and electric field

$$j_x(\omega_L) = n_s n_v e v_F \sum_{\mathbf{k}} \int_\tau^{\tau + \frac{2\pi}{\omega_L}} \text{Tr}(\rho_{\mathbf{k}}(t)\sigma_x) e^{i\omega_L t} dt, \qquad (8)$$

$$E_x(\omega_L) = \int_\tau^{\tau + \frac{2\pi}{\omega_L}} (E_d \cos(\omega_d t) + E_L \sin(\omega_L t)) e^{i\omega_L t} dt, \qquad (9)$$

where τ is a point in time where the system has reached its steady state. $n_s = n_v = 2$ are the spin- and valley-degeneracies. e is the electron charge. $\sigma_r(\omega_L)$ is obtained for the probing field $E_L = 10$ V m^{-1}. We have verified that the conductivity obtained in this manner is the linear response and that the sum over k includes sufficiently many points surrounding the Dirac point.

As we demonstrate in Fig. 2a, $\sigma_r(\omega_L)$ displays resonant features that match the band gaps of the Floquet spectrum. The energy gap Δ_0 increases with increasing field strength E_d, in a

3
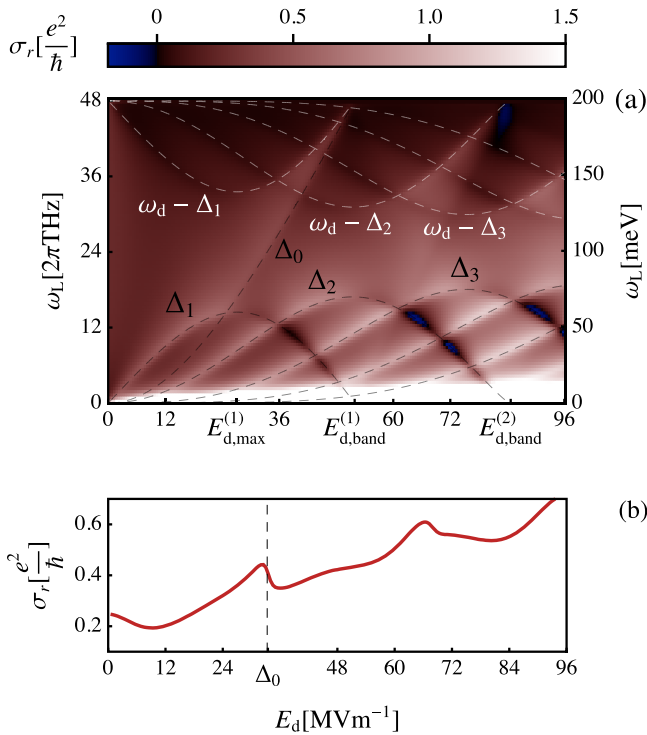
Fig. 2 Longitudinal optical conductivity of light-driven graphene. The real part of the optical conductivity of graphene driven at the frequency $\omega_d = 2\pi \times 48$ THz ≈ 200 meV as a function of the driving field strength E_d (a) and a cut at half the driving frequency $\omega_L = \omega_d/2 = 2\pi \times 24$ THz (b). The dashed lines show the various band gaps Δ_m as given by Floquet theory. The gap Δ_0 becomes clearly visible above values of $\omega_L \approx 2\pi \times 14$ THz ≈ 60 meV and $E_d \approx 28$ MV m^{-1}. We also see the complementary resonant features at $\omega_d - \Delta_m$, with $m > 0$.

Fig. 3 Electron distribution at the Dirac point. The electron distribution $n(k = 0, \omega)$ at the Dirac point as a function of the driving field strength E_d. The driving frequency is $\omega_d = 2\pi \times 48$ THz ≈ 200 meV. The scaling behavior of the gap at the Dirac point is $\Delta_0 = 2\sqrt{v_F^2 E_d^2/\omega_d^2 + \omega_d^2/4} - \omega_d$, where v_F is the Fermi velocity. The vertical dotted line indicates $E_d = E_{d,band}^{(1)}$. The horizontal dotted lines indicate Floquet zone boundaries. The dashed lines show the Floquet energies at the Dirac point (See Supplementary Note 1) that are formally constrained to be inside the first Floquet zone. The occupations stay confined within the Floquet bands adiabatically connected to the bare graphene and one replica outwards. There are no complementary gaps at $k = 0$.
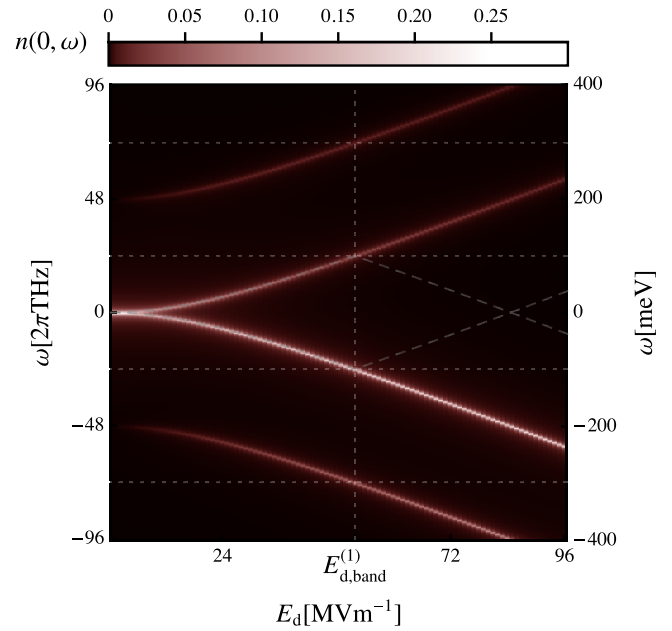
monotonuous fashion. The energy gaps Δ_m, with $m > 0$, first increase with E_d, then reach a maximum at $E_d = E_{d,max}^{(m)}$, then decrease, and ultimately reach 0 at $E_d = E_{d,band}^{(m)}$. At this driving strength the gap is located at $k = 0$ and merges with Δ_0.

The magnitude of $\sigma_r(\omega_L)$ at the resonance Δ_1, i.e., the magnitude of $\sigma_r(\Delta_1)$, displays a maximum for $E_d < E_{d,max}^{(1)}$, relative to its background, and a minimum for $E_d > E_{d,max}^{(1)}$. The magnitude of $\sigma_r(\omega_L)$ at $\omega_d - \Delta_1$, displays the complementary behavior. $\sigma_r(\omega_d - \Delta_1)$ has a minimum for $E_d < E_{d,max}^{(1)}$, and a maximum for $E_d > E_{d,max}^{(1)}$. Note that this does not happen for Δ_0 due to the lack of a complementary gap $\omega_d - \Delta_0$ as can be seen in Figs. 1 and 3.

We note that in the limit of $E_d \to 0$, the optical conductivity $\sigma_r(\omega_L)$ approaches the value $\frac{1}{4}\frac{e^2}{\hbar}$ for non-zero frequencies. An example for this is visible in Fig. 2b, for $\omega_L = 2\pi \times 24$ THz. Additionally, we obtain a peak at $\omega_L = 0$, which is the Drude peak broadened by the dissipative terms. We show the real part of the longitudinal conductivity $\sigma_r(\omega_L)$ for $E_d = 0$ in Supplementary Note 2.

We obtain analytical expressions for Δ_0 and $E_{d,band}^{(m)}$ by considering the Hamiltonian in Eq. (2) at the Dirac point and without probing, i.e., $k = 0$ and $E_L = 0$. This has the time-dependent Rabi solutions

$$|+\rangle \sim e^{i(\omega_d t/2 + \pi/4)} \begin{pmatrix} \cos(\Omega t) - \frac{i\omega_d \sin(\Omega t)}{2\Omega} \\ e^{-i\omega_d t}\frac{E_d \sin(\Omega t)}{\Omega \omega} \end{pmatrix}, \quad (10)$$

$$|-\rangle \sim e^{-i(\omega_d t/2 + \pi/4)} \begin{pmatrix} -e^{i\omega_d t}\frac{E_d \sin(\Omega t)}{\Omega \omega_d} \\ \cos(\Omega t) + \frac{i\omega_d \sin(\Omega t)}{2\Omega} \end{pmatrix}, \quad (11)$$

where

$$\Omega = \sqrt{\frac{v_F^2 E_d^2}{\omega_d^2} + \frac{\omega_d^2}{4}}. \quad (12)$$

The gap at the Dirac point is given by $\Delta_0 = 2\Omega - \omega_d$. This expression is also the Aharanov-Anandan phase of this system[2]. In the weak driving limit this gap follows the expected perturbative behavior[11] $\Delta_0 \approx v_F^2 E_d^2/\omega_d^3$ whereas in the strong driving limit it develops a linear dependence on E_d as $\Delta_0 \approx v_F E_d/\omega_d$. We use the full expression for Δ_0 to find the driving strengths $E_{d,band}^{(m)}$, since they occur whenever the gap Δ_0 spans a multiple of ω_d. By setting $2\Omega - \omega_d = m\omega_d$, $m \in \mathbb{N}$, we find

$$E_{d,band}^{(m)} = v_F^{-1}\sqrt{\frac{m}{2} + \frac{m^2}{4}}\omega_d^2. \quad (13)$$

We display the Dirac gap in Fig. 3, and compare it to the electron distribution at $\mathbf{k} = 0$, of the steady state. We observe that the two maxima of the electron distribution that emerge from $\omega = 0$ follow the prediction of $\pm\Delta_0$, even as Δ_0 grows larger than the Floquet zone boundary at ω_d. Therefore, Δ_0 is a more natural energy scale to predict the resonances at $\mathbf{k} = 0$ for large driving intensities, than the direct band gap that is strictly smaller than ω_d. For increasing field strength E_d, the occupation of the upper
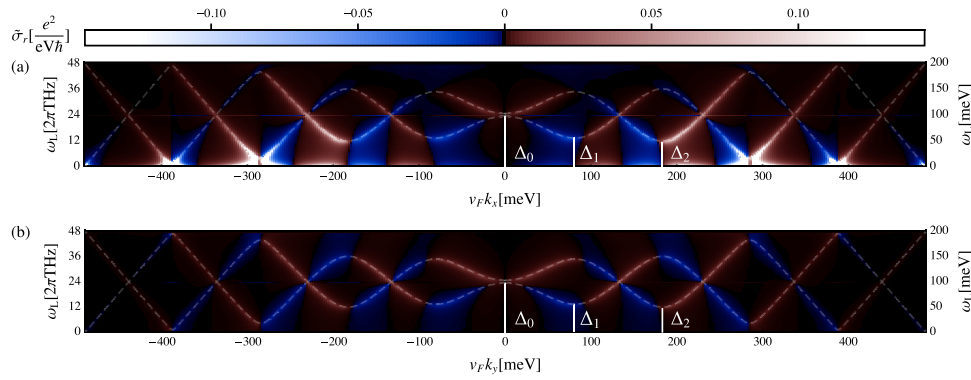
Fig. 4 Momentum-resolved optical conductivity of light-driven graphene. The momentum-resolved contributions to the optical conductivity of driven graphene along the k_x (**a**) and k_y (**b**) momentum directions. The driving frequency is $\omega_d = 2\pi \times 48$ THz ≈ 200 meV and the field strength is $E_d = 34$ MV m^{-1}. For these parameters the gap at the Dirac point roughly matches half the driving frequency such that $\Delta_0 \approx \omega_d/2$. The dashed lines indicate the Floquet band energy differences $\Delta\epsilon(k)$ and $\omega_d - \Delta\epsilon(k)$ (See Supplementary Note 1).

two bands decreases. The occupation of complementary gaps is zero throughout Fig. 3.

As visible in Fig. 2a, the conductivity vanishes around the probing frequency $\omega_L \approx 2\pi \times 12$ THz ≈ 50 meV and the driving field strength of $E_d \approx 39$ MV m^{-1}. Here the first gap Δ_1 decreases with increasing E_d and creates a negative contribution that suppresses $\sigma_r(\omega_L)$ to zero. For higher order gaps, e.g., Δ_2 and Δ_3 in Fig. 2a, the same phenomenon even leads to a sign change in the conductivity. Whenever a gap is in the regime of decreasing with increasing E_d, and no other resonance contributes positively and too strongly to the conductivity, the negative contributions can cancel the background and result in net negative optical conductivity. Such a total negative conductivity in the system amounts to an out-of-phase response to a probing field with a probing frequency in the regime in which $\sigma_r(\omega_L)$ is negative. In principle this can be utilized to obtain electrical gain out of the system, where the required energy is effectively taken from the driving.

Momentum-resolved conductivity. In order to gain further insight into the origin of the features in the total optical conductivity shown in Fig. 2, we explore the momentum resolved contributions to the conductivity. In Fig. 4 we resolve the contributions to the conductivity along the k_x and k_y directions relative to the Dirac point in momentum space, defined as

$$\tilde{\sigma}_r(\mathbf{k}, \omega_L) = \frac{n_s n_v e v_F |\mathbf{k}|}{E_x(\omega_L)} \int_{\tau}^{\tau + \frac{2\pi}{\omega_L}} \mathrm{Tr}(\rho_{\mathbf{k}}(t)\sigma_x)e^{i\omega_L t}dt. \quad (14)$$

Here, we include the linear scaling with the absolute momenta $|\mathbf{k}|$ in polar coordinates. Direct interband transitions between neighboring Floquet bands give rise to resonant features in $\tilde{\sigma}_r(\mathbf{k}, \omega_L)$ that match the Floquet band energy differences $\Delta\epsilon(k)$ and $\omega_d - \Delta\epsilon(k)$ (See Supplementary Note 1). These resonant features contribute to the conductivity with alternating signs. The sign changes occur close to the band gap locations, but slightly shifted towards (away from) the Dirac point in case the gap size increases (decreases) with respect to the field strength E_d. For gaps that do not change with respect to E_d, i.e., gaps at their maximum, this shift vanishes. Therefore, the accumulated contributions across gaps net either positive or negative conductivity depending on the change in gap size with respect to field strength E_d. This is consistent with the enhancements and reductions in $\sigma_r(\omega_L)$ at the gaps Δ_m, with $m > 0$, and their complementary gaps $\omega_d - \Delta_m$, seen in Fig. 2a.

For probing frequencies ω_L that are not resonant with a given band gap, $\tilde{\sigma}_r(\mathbf{k}, \omega_L)$ does not vanish in general. This results in a background conductivity that can obscure the gap Δ_0 at the Dirac point in particular, as is the case for $E_d < E_{d,max}^{(1)}$ in Fig. 2a. Since the band gaps Δ_m, with $m > 0$, and their complementary gaps $\omega_d - \Delta_m$ have a maximum at the field strength $E_d = E_{d,max}^{(m)}$, there is always a range that no gap Δ_m, with $m > 0$, reaches that is centered around $\omega_L = \omega_d/2$. In this range, it is the gap Δ_0 that is visible predominantly. The overall behavior of the gaps is self-similar with respect to the driving frequency ω_d. Therefore in this system, there always exists a reliable range of probing frequencies where the gap Δ_0 can be observed.

The Floquet interband transitions resonant with $\Delta\epsilon(k)$ occur inside a given Floquet zone. The ones resonant with $\omega_d - \Delta\epsilon(k)$ occur across Floquet zone boundaries. Hence, we refer to them as intra-Floquet $\tilde{\sigma}_r^{\mathrm{intra}}(\mathbf{k}, \omega_L)$ and inter-Floquet $\tilde{\sigma}_r^{\mathrm{inter}}(\mathbf{k}, \omega_L)$ contributions to the conductivity, respectively. To distinguish the two we write

$$\tilde{\sigma}_r(\mathbf{k}, \omega_L) = \tilde{\sigma}_r^{\mathrm{intra}}(\mathbf{k}, \omega_L) + \tilde{\sigma}_r^{\mathrm{inter}}(\mathbf{k}, \omega_L) + \tilde{\sigma}_r^{\mathrm{bg}}(\mathbf{k}, \omega_L), \quad (15)$$

where $\tilde{\sigma}_r^{\mathrm{bg}}(\mathbf{k}, \omega_L)$ is a remaining background contribution accounting for the $\omega_L \to 0$ behavior in $\tilde{\sigma}_r(\mathbf{k}, \omega_L)$. Figure 4b shows that $\sigma_r^{\mathrm{bg}}(k_y, \omega_L) \approx 0$. We fit a function of two Lorentzians located at $\Delta\epsilon(k)$ and $\omega_d - \Delta\epsilon(k)$ with the same fixed width $\Gamma = 1$ THz to the numerical results of $\tilde{\sigma}_r(k_y, \omega_L)$. Specifically, we use

$$\tilde{\sigma}_r^{\mathrm{fit}}(k_y, \omega_L) = \frac{\Gamma}{\pi} \frac{\tilde{\sigma}_r^{\mathrm{intra}}(k_y)}{\Gamma^2 + (\omega_L - \Delta\epsilon)^2}$$
$$+ \frac{\Gamma}{\pi} \frac{\tilde{\sigma}_r^{\mathrm{inter}}(k_y)}{\Gamma^2 + (\omega_L - \omega_d + \Delta\epsilon)^2} \quad (16)$$

as a fitting function.

The conductivity features derive from the transitions between the Floquet bands, and are therefore related to the occupation of these bands. We define the relative occupation

$$\Delta n(k) = \sum_{m \in \mathbb{Z}} n_m^-(k) - n_m^+(k), \quad (17)$$

where $n_m^\pm(k)$ is the occupation at momentum k of the mth upper (lower) Floquet band given by integrating $n(k, \omega)$ from $(m - \frac{1}{4} \pm \frac{1}{4})\omega_d$ to $(m + \frac{1}{4} \pm \frac{1}{4})\omega_d$.

Figure 5 shows the momentum-resolved intra-Floquet conductivity $\tilde{\sigma}_r^{\mathrm{intra}}(k_y)$ which is determined via fitting as described above, as well as the effective relative occupation $\Delta n(k)$ of the
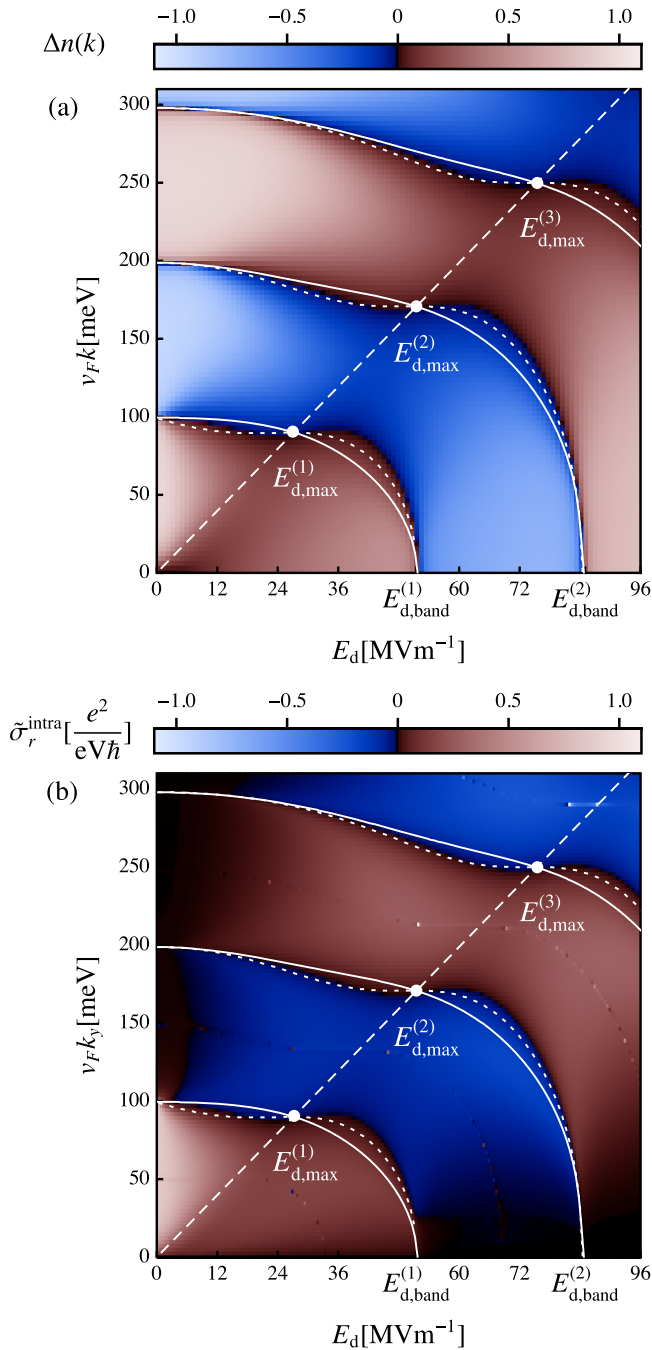
Fig. 5 Effective Floquet state occupation and intra-Floquet conductivity. The effective occupation $\Delta n(k)$ (**a**) and the fitted intra-Floquet conductivity $\tilde{\sigma}_r^{\text{intra}}(k_y)$ (**b**) as functions of the field strength E_d. The solid white lines are given by the locations in momentum space of the band gaps Δ_m, with $m > 0$. The dotted white lines are given by the zero-crossings of a type of comoving band velocity $\partial_\Pi \Delta\epsilon = 0$, where $\Pi = v_F(k + E_d/\omega_d)$ (See Supplementary Note 1). The dashed line is given by $k = \frac{E_d}{\omega_d}$.

Floquet bands as functions of the field strength E_d. They are in good qualitative agreement with each other. Both quantities display tongues with alternating signs and zero-crossings seperating them that agree very well between $\Delta n(k)$ and $\tilde{\sigma}_r^{\text{intra}}(k_y)$. The zero-crossings touch the $v_F\,k$-axis at $m\omega_d/2$ and the E_d-axis at $E_{d,\text{band}}^{(m)}$, $m \in \mathbb{N}$. The solid white lines show the location of the Floquet band gaps, i.e., where the radial band

velocity vanishes, i.e., $\partial_k\,\epsilon = 0$. They roughly follow the zero-crossings of $\Delta n(k)$ and $\tilde{\sigma}_r^{\text{intra}}(k_y)$ while showing small, but clear deviations. We observe that for $E_{d,\text{max}}^{(m)} < E_d < E_{d,\text{band}}^{(m)}$ the steady state displays an inversion of the Floquet bands, which creates a negative contribution to the optical conductivity. The dotted white lines indicate where the comoving radial band velocity $\partial_\Pi \epsilon$ with $\Pi = v_F(k + E_d/\omega_d)$ vanishes, i.e., $\partial_\Pi \epsilon = 0$. These lines show improved agreement with the zero-crossings of $\Delta n(k)$ and $\tilde{\sigma}_r^{\text{intra}}(k_y)$. Further, there is an overall resemblance between $\partial_\Pi \epsilon(k)$, $\Delta n(k)$, and $\tilde{\sigma}_r^{\text{intra}}(k_y)$ (See Supplementary Note 1).

We summarize that the momentum-resolved optical conductivity shows two types of interband processes across the effective Floquet band structure. These resonant processes correspond to the energy differences $\Delta\epsilon(k)$ and $\omega_d - \Delta\epsilon(k)$ between Floquet bands and contribute both positively and negatively. We relate these conductivities to the effective relative occupation of the Floquet bands $\Delta n(k)$. We find that effective inversions of the Floquet bands correspond to reductions in the conductivity which can lead to a sign change in the total optical conductivity. These band inversions at the Floquet gaps and their reductions of the optical conductivity systematically occur in regimes of decreasing gap sizes with respect to the driving field strength.

Conclusion

In conclusion, we have proposed the longitudinal optical conductivity of illuminated graphene as a realistic observable to detect Floquet band gaps. We have shown that this quantity displays the Floquet gaps as functions of the driving intensity and the probing frequency. In particular, we have pointed out a regime in which the band gap at the Dirac point can be detected. All band gaps except for the band gap at the Dirac point, first increase with the driving intensity, approach a maximal value, and then decrease. For the increasing regime, the optical conductivity displays a positive contribution. For the decreasing regime, it displays a negative contribution that can amount to a total negative conductivity at the given frequency. We point out that this negative contribution derives from an inversion of the occupation of the Floquet bands. Therefore, the proposed experiment not only provides an unambiguous detection of Floquet bands, but also demonstrates dynamical control of transport in solids with light.

Methods

Driven graphene dynamics. We express the driven graphene Hamiltonian in a four-level description, spanned by the states $|0\rangle$, $c_{k,A}^\dagger|0\rangle$, $c_{k,B}^\dagger|0\rangle$ and $c_{k,B}^\dagger c_{k,A}^\dagger|0\rangle$. The $c_{k,A/B}^{(\dagger)}$ are the annihilation (creation) operators at the momentum k in the sublattice A/B. The Hamiltonian H is defined in Eq. (1). We factorize the density matrix in momentum space as $\rho = \Pi_k \rho_k$ and simulate the dissipative dynamics using the Lindblad-von Neumann master equation

$$\dot{\rho} = i[\rho, H] + \sum_j c_j\left(L_j \rho L_j^\dagger - \frac{1}{2}\{L_j^\dagger L_j, \rho\}\right),$$

where the sum over j goes over the momentum-dependent Lindblad operators

$$L_z = V(c_{k,A}^\dagger c_{k,A} - c_{k,B}^\dagger c_{k,B})V^\dagger$$
$$L_+ = V(c_{k,B}^\dagger c_{k,A})V^\dagger$$
$$L_- = V(c_{k,A}^\dagger c_{k,B})V^\dagger$$
$$L_l = V\begin{pmatrix} 0 & \delta_{l,-1} & \delta_{l,-2} & 0 \\ \delta_{l,1} & 0 & 0 & \delta_{l,-3} \\ \delta_{l,2} & 0 & 0 & \delta_{l,-4} \\ 0 & \delta_{l,3} & \delta_{l,4} & 0 \end{pmatrix}V^\dagger$$

with $l = \pm 1, \pm 2, \pm 3, \pm 4$. $\delta_{l,i}$ is the Kronecker-Delta and V is the transformation into the instantaneous eigenbasis of $\mathbf{h}(k)$ defined in Eq. (2). The dissipation coefficients

c_j fulfill the conditions

$$c_z = \gamma_z$$
$$c_+ + c_- = \gamma_- \qquad c_+ = c_- \exp\{-2\epsilon\beta\}$$
$$c_1 + c_{-1} = \gamma_{bg} \qquad c_{-1} = c_1 \exp\{+\epsilon\beta\}$$
$$c_2 + c_{-2} = \gamma_{bg} \qquad c_{-2} = c_2 \exp\{-\epsilon\beta\}$$
$$c_3 + c_{-3} = \gamma_{bg} \qquad c_{-3} = c_3 \exp\{-\epsilon\beta\}$$
$$c_4 + c_{-4} = \gamma_{bg} \qquad c_{-4} = c_4 \exp\{+\epsilon\beta\}$$

with $\beta = (k_B T)^{-1}$. $\pm\epsilon$ are the instantaneous eigenenergies of $\mathbf{h}(\mathbf{k})$. This approach is also detailed in previous work[12].

In order to calculate the electron distribution, we first calculate the two-point correlation functions $\langle c_{\mathbf{k},i}^\dagger(t_2) c_{\mathbf{k},i}(t_1) \rangle$. We do this by acting with $c_{\mathbf{k},i}$ on the density matrix $\rho_{\mathbf{k}}(t_1)$ and continuing the time-evolution with the same master equation until the time t_2 at which we act on the resulting density with the operator $c_{\mathbf{k},i}^\dagger$. We do this for all pairs of times t_1 and t_2 in the interval $[\tau_1, \tau_2]$ and calculate the electron distribution as detailed in Eq. (5).

Data availability
The data that support the findings of this study are available from the corresponding author upon reasonable request.

Code availability
The code used to generate the data presented in this study is available from the corresponding author upon reasonable request.

References

1. Basov, D. N., Averitt, R. D. & Hsieh, D. Towards properties on demand in quantum materials. *Nat. Mater.* **16**, 1077–1088 (2017).
2. Oka, T. & Kitamura, S. Floquet engineering of quantum materials. *Tech. Rep.* https://doi.org/10.1146/annurev-conmatphys-031218-013423 (2019).
3. Wackerl, M., Wenk, P. & Schliemann, J. Floquet-drude conductivity. *Phys. Rev. B* **101**, 184204 (2020).
4. Chen, Q., Du, L. & Fiete, G. A. Floquet band structure of a semi-dirac system. *Phys. Rev. B* **97**, 035422 (2018).
5. Kitagawa, T., Oka, T., Brataas, A., Fu, L. & Demler, E. Transport properties of nonequilibrium systems under the application of light: photoinduced quantum hall insulators without landau levels. *Phys. Rev. B* **84**, 235108 (2011).
6. Lindner, N. H., Refael, G. & Galitski, V. Floquet topological insulator in semiconductor quantum wells. *Nat. Phys.* **7**, 490–495 (2011).
7. Rudner, M. & Lindner, N. Band structure engineering and non-equilibrium dynamics in floquet topological insulators. *Nat. Rev. Phys.* **2**, 229–244 (2020).
8. Sameti, M. & Hartmann, M. J. Floquet engineering in superconducting circuits: from arbitrary spin-spin interactions to the kitaev honeycomb model. *Phys. Rev. A* **99**, 012333 (2019).
9. Žutić, I., Fabian, J. & Das Sarma, S. Spintronics: fundamentals and applications. *Rev. Mod. Phys.* **76**, 323–410 (2004).
10. Haldane, F. D. M. Model for a quantum hall effect without landau levels: condensed-matter realization of the "parity anomaly". *Phys. Rev. Lett.* **61**, 2015–2018 (1988).
11. Oka, T. & Aoki, H. Photovoltaic hall effect in graphene. *Phys. Rev. B* **79**, 081406 (2009).
12. Nuske, M. et al. Floquet dynamics in light-driven solids. *Phys. Rev. Res.* **2**, 043408 (2020).
13. McIver, J. W. et al. Light-induced anomalous hall effect in graphene. *Nat. Phys.* **16**, 38–41 (2019).
14. Fläschner, N. et al. Experimental reconstruction of the berry curvature in a floquet bloch band. *Science* **352**, 1091–1094 (2016).
15. Jotzu, G. et al. Experimental realization of the topological haldane model with ultracold fermions. *Nature* **515**, 237–240 (2014).
16. Aidelsburger, M. et al. Realization of the hofstadter hamiltonian with ultracold atoms in optical lattices. *Phys. Rev. Lett.* **111**, 185301 (2013).
17. Rechtsman, M. C. et al. Photonic floquet topological insulators. *Nature* **496**, 196–200 (2013).
18. Mukherjee, S. et al. Experimental observation of anomalous topological edge modes in a slowly driven photonic lattice. *Nat. Commun.* **8**, 13918 (2017).
19. Ma, G., Xiao, M. & Chan, C. T. Topological phases in acoustic and mechanical systems. *Nat. Rev. Phys.* **1**, 281–294 (2019).
20. Wang, Y. H., Steinberg, H., Jarillo-Herrero, P. & Gedik, N. Observation of floquet-bloch states on the surface of a topological insulator. *Science* **342**, 453–457 (2013).
21. Schüler, M. et al. How circular dichroism in time- and angle-resolved photoemission can be used to spectroscopically detect transient topological states in graphene. *Phys. Rev. X* **10**, 041013 (2020).
22. Sentef, M. A. et al. Theory of floquet band formation and local pseudospin textures in pump-probe photoemission of graphene. *Nat. Commun.* **6**, 7047 (2015).
23. Keunecke, M. et al. Direct access to auger recombination in graphene (2020). https://arxiv.org/abs/2012.01256 (2020).
24. Aeschlimann, S. et al. Survival of floquet-bloch states in the presence of scattering. *Nano Lett.* **21**, 5028–5035 (2021).
25. Kumar, A., Rodriguez-Vega, M., Pereg-Barnea, T. & Seradjeh, B. Linear response theory and optical conductivity of floquet topological insulators. *Phys. Rev. B* **101**, 174314 (2020).
26. Zhou, Y. & Wu, M. W. Optical response of graphene under intense terahertz fields. *Phys. Rev. B* **83**, 245436 (2011).
27. Freericks, J. K., Krishnamurthy, H. R. & Pruschke, T. Theoretical description of time-resolved photoemission spectroscopy: application to pump-probe experiments. *Phys. Rev. Lett.* **102**, 136401 (2009).

Author contributions
L.B. and L.M. conceived the project. L.B. performed the calculations, simulations, and analysis, supervised by L.M.

Competing interests
The authors declare no competing interests.

Additional information
Supplementary information The online version contains supplementary material available at https://doi.org/10.1038/s42005-021-00746-6.

Correspondence and requests for materials should be addressed to Lukas Broers.

Peer review information Communications Physics thanks the anonymous reviewers for their contribution to the peer review of this work. Peer reviewer reports are available.

Reprints and permission information is available at http://www.nature.com/reprints

Publisher's note Springer Nature remains neutral with regard to jurisdictional claims in published maps and institutional affiliations.